Fully Kinetic Modeling of a Divergent Cusped-Field Thruster

by

Stephen R. Gildea

Submitted to the Department of Aeronautics and Astronautics
in partial fulfillment of the requirements for the degree of

Master of Science in Aeronautics and Astronautics

at the

MASSACHUSETTS INSTITUTE OF TECHNOLOGY

September 2009

Author .....
Department of Aeronautics and Astronautics
August 20, 2009

Certified by...
Manuel Martínez-Sánchez
Professor
Thesis Supervisor

Accepted by .....
David L. Darmofal
Professor
Associate Department Head
Chair, Committee on Graduate Students

Fully Kinetic Modeling of a Divergent Cusped-Field Thruster

by

Stephen R. Gildea

Submitted to the Department of Aeronautics and Astronautics
on August 20, 2009, in partial fulfillment of the
requirements for the degree of
Master of Science in Aeronautics and Astronautics

Abstract

A fully kinetic, particle-in-cell plasma simulation tool has been incrementally developed by members of the Massachusetts Institute of Technology Space Propulsion Laboratory. Adapting this model to simulate the performance and plasma dynamics of a divergent cusped-field thruster is discussed. Strong magnetic fields in the cusps (B≈0.5 T) necessitate using a time step on the order of a picosecond in order to resolve electron cyclotron trajectories. As a result, successfully completing a divergent cusped-field thruster simulation with the full magnetic field strength has yet to be accomplished. As an intermediate step, simulation results of a divergent cusped-field thruster with the magnetic field at 1/5 the actual value are presented, including performance parameters and internal plasma structure details. Evidence suggests that even at 1/5 the magnetic field strength, ions are fully magnetized within certain regions of the divergent cusped-field thruster. This has strong implications concerning the basic operating principles of the thruster because the Hall effect does not result in a net flow of current in regions where ions are fully magnetized. Further modifications that may lead to successful simulations of divergent cusped-field thrusters at full magnetic field strength are also outlined, which may allow for more detailed studies of the plasma structure and performance of the cusped-field thruster.

Thesis Supervisor: Manuel Martínez-Sánchez
Title: Professor

Acknowledgments

I would like to thank my advisor, Professor Martínez-Sánchez, for always making himself available for discussion. Also, this project could not have been completed without the valuable insights of Dr. Oleg Batishchev. I want to thank him for continually providing me with new perspectives on what it means to execute and interpret a kinetic simulation. Dr. James Szabo and Dr. Justin Fox were also helpful when the only people left to ask were the authors of the code.

I would also like to thank the administrators and everyone involved with the Science Mathematics and Research for Transformation Scholarship Program. This program has truly been a catalyst for exciting scientific opportunities.

Above all, I would like to thank my wife, Erin, for her unending support, strength and love.

Contents

List of Figures

List of Tables

Chapter 1

Introduction to Divergent Cusped-Field Thrusters

1.1 Cusped-Field Thrusters

Stationary plasma type (SPT) Hall thrusters have been operated in earth orbit since 1972[3] with typical efficiencies near 50% and a specific impulse of 1600 s[4]. However, the operational lifetime of SPT Hall thrusters is often limited by erosion of dielectric material used to provide insulation from the plasma[5]. Researchers at the Massachusetts Institute of Technology (MIT) Space Propulsion Laboratory (SPL) began investigating divergent cusped-field (DCF) thrusters[1, 2, 6] to determine their promise as a longer lifetime alternative to existing low power Hall thrusters. Other cusped-field thrusters include the High Efficiency Multi-stage Plasma (HEMP) thrusters patented by THALES Electron Devices[7, 8, 9] and the Cylindrical Hall Thruster (CHT) developed at the Princeton University Electric Propulsion & Plasma Dynamics Laboratory[10]. A detailed comparison of the DCFT design to the HEMP, CHT, and other cusped-field devices is provided by Courtney *et al.*[6].

1.2 Divergent Cusped-Field Thrusters

DCF thrusters are electric propulsion devices characterized by a divergent, dielectric wall channel and a magnetic topology dominated by two magnetic cusps and a magnetic bottle near the anode (see Figure 3-3). The magnetic circuit consists of three annular samarium cobalt (SmCo) permanent magnets arranged such that like poles face one another, and a

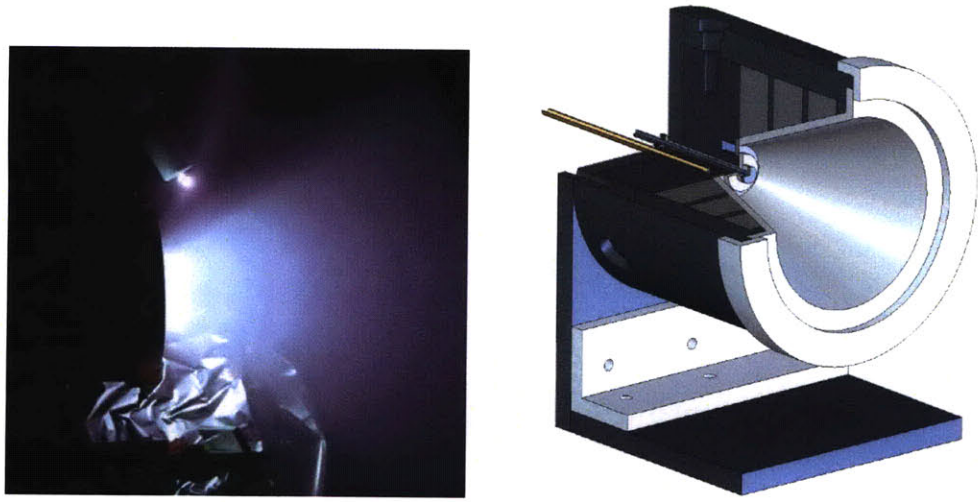

(a) DCFT firing.[1]

(b) 3D Engineering Model of DCFT with an angled section.[2]

Figure 1-1: DCFT Visualizations.

core at the base of the thruster composed of 1018 carbon steel (see Figure 1-1(b)). Xenon gas is injected 5 mm upstream from the downstream face of the anode through a porous, stainless steel disc embedded in the magnetic core. In this way, the neutral injection and anode locations are decoupled from one another in the Divergent Cusped-Field Thruster (DCFT) design. For complete details of the DCFT and existing data, please consult previous studies[2, 1, 6, 11]. Existing experimental data[2, 1, 6] catalogues DCFT performance (anode specific impulse, thrust, anode thrust efficiency) at operating conditions ranging between 100 W to 500 W, with a nominal operating condition corresponding to a xenon flow rate of 8.5 sccm and an applied anode voltage of 550 V. At this operating point, the DCFT consumes 242 W of power, and produces 13.4 mN of thrust while operating with an anode thrust efficiency of 44.5%. Although basic DCFT operating principles are thought to include azimuthal electron currents within regions characterized by radial magnetic fields, the competing roles that strong magnetic bottles and internal electric fields play in determining the location and efficiency of ionization (whether in the upstream cusp, downstream cusp, or both) have yet to be explicitly measured in experiments or rigourously explained based on theoretical arguments or simulation results. Demonstrating the effectiveness of the magnetic topology and divergent chamber geometry as erosion barriers remains unachieved as well. The goal of the present investigation is to gain a deeper understanding of underlying mechanisms at play within cusped-field thrusters using a fully kinetic, particle-in-cell

computational model of the DCFT. This simulation tool will be benchmarked against detailed DCFT experimental measurements (completed by members of the MIT SPL[11], Air Force Research Laboratory and Stanford Plasma Physics Laboratory). A working model will help evaluate how design decisions will affect performance metrics such as plume divergence angle, ionization efficiency, ion energy efficiency, and the spatially resolved energy flux to DCFT chamber surfaces. Figure 1-1(a) shows the first successful firing of the DCFT at the MIT SPL.

Chapter 2

Introduction to Fully Kinetic Modeling

Fully kinetic modeling refers to representing a fluid as discrete particles whose trajectories are dynamically simulated. Specifying the type (mass, charge, etc.) and state (position and velocity) of each particle at a given instant in time allows the state of each particle to be determined at any future time by integrating the equation of motion for each particle under the influence of known forces. Knowledge of the state of each member in a set of particles allows the velocity distribution function for each species to be tabulated at each location in the simulation domain. The velocity distribution function links the view of a fluid as a discrete set of particles to that of a continuum; providing the density, bulk velocity and temperature of each species as moments of the velocity distribution function.

The present work considers electromagnetic forces acting on neutral particles, ions and electrons. Additionally, the trajectories of particles are strongly influenced by collisions with other particles and boundaries. The details of how these forces and interactions are accounted for are provided in Chapter 3, and references cited throughout.

2.1 Modeling Plasma Thrusters

Modeling plasma systems is an ongoing effort of research throughout the scientific community. However, the following narrative focuses on the development of models for Hall Thrusters within the Space Propulsion Laboratory at the Massachusetts Institute of Technology, as they are by far the most relevant.

In 1995, Fife provided a simulation tool to model the performance and plasma dynamics of Hall Thrusters[12]. Neutrals and ions were modeled as particles within a two-dimensional (R-Z plane), nonorthogonal, structured mesh (hence, Particle-in-Cell). Conversely, the electron velocity distribution function was everywhere assumed to be Maxwellian and the electrons were governed by fluid equations. The model was refined and compared to experimental measurements in 1999[13].

Due to errors attributed to the assumption of an isotropic electron velocity distribution function, Szabo expanded the Particle-in-Cell (PIC) approach to include electrons in 2001[14]. Although the spatial dimensionality of the model remained the same, velocities of all particles were accounted for in three dimensions (2D3V). Later, the model was modified to include dielectric boundaries[15] and used to conduct an investigation into wall erosion on high powered Hall Thrusters[16].

In order to make implementations more tractable for higher powered thrusters, Fox parallelized the method in 2007[17], allowing for the growing availability of parallel computing hardware to be exploited. Fox added the additional capability of the analytical quench model[18, 19, 20] in an attempt to self-consistently account for anomalous electron diffusion[21]. Additional features that Fox added to the code, such as an adaptive meshing capability, are not present in the version used in this investigation.

2.2 Feasible Implementation of the Kinetic Method

The computational resources necessary to perform a complete, kinetic simulation are well beyond the capabilities of contemporary technology. The DCFT will be used as an example to justify this assertion:

- On the order of 10^{13} particles need to be simulated for an assumed average number density of 10^{12} per ccm. For a 2D3V simulation, that means integrating 5×10^{13} scalar differential equations each time step!

- Maintaining numerical stability requires the largest allowable time step to be the inverse of the largest characteristic frequency in the domain. Using the previously assumed number density, and a maximum magnetic field of .53 T[2], the time steps based on the electron plasma and cyclotron frequencies are on the order of 1 ps and 10 ps, respectively. Simulating the residence time of a neutral Xenon population with

a temperature of 1000 K (DCFT chamber length is about 5 cm) requires about 2×10^8 iterations.

- For a plasma number density on the order of 10^{12} per ccm and an electron temperature of 20 eV, a representative electron Debye length for the DCFT is 30 μm. Resolving the Debye length, a necessary condition for numerical stability, requires a mesh with about 10^{10} nodes. Therefore, determining the potential distribution for a single iteration requires the solution of a system with approximately 10^{10} unknowns.

Even under the assumption that each action above (integrating one equation of motion or solving the potential of a single node) could be accomplished with a single floating point operation, and that using additional processors produces an idealized speed up factor of (1/n), the time required to run the simulation on a parallel machine with 100, 1 GHz processors would still be over 3000 years[1]! Fortunately, Szabo developed a methodology[14] that vastly reduces the necessary computational resources while still providing credible simulation results.

2.2.1 Reducing the Problem Size and Accelerating Convergence

Szabo's model modifies selected fundamental physical quantities associated with plasma systems in order to reduce the computational scale of the problem, and then takes additional steps to convert quantities in the artificial system to those that would be measured in a real plasma. Full details of Szabo's method are presented in Reference [14], with the most daring assumption being that the bulk quantities of temperature (T) and number density (n) remain unaffected by the changes outlined in the remainder of this chapter[2].

Increasing Free Space Permittivity: γ

Equation 2.1 shows how the permittivity of free space (ϵ_o) is modified within the simulation. The value of γ is specified in an input file by the user.

$$\epsilon_o^* \equiv \gamma^2 \epsilon_o \tag{2.1}$$

[1]This estimate also assumes the machine has enough RAM to store the entire simulation as it runs.

[2]Consequently, $T^* \equiv T$ and $n^* \equiv n$. The superscript * will be used throughout to indicate simulated values of a quantity, whereas variables lacking the asterisk would be the 'real' value.

Increasing the free space permittivity has two beneficial consequences related to reducing the enormity of the required simulation task. Equations 2.2 and 2.3 illustrate how the length and time scales that govern the behavior of the simulation are both increased by the factor γ.

$$\lambda^*_{D,e} = \sqrt{\frac{\epsilon^*_o kT}{e^2 n_e}} = \gamma(\lambda_{D,e}) \tag{2.2}$$

$$\omega^*_{p,e} = \sqrt{\frac{e^2 n_e}{\epsilon^*_o m_e}} = \frac{\omega_{p,e}}{\gamma} \tag{2.3}$$

An important caveat is that the simulation time scale will only increase if the modified electron plasma frequency continues to be the largest characteristic frequency in the domain. For instance, the electron cyclotron frequency is unchanged by any of the altered quantities in Szabo's method, meaning a reduction in the electron plasma frequency by a certain factor will eventually cause the electron cyclotron frequency to dominate. At this point, increasing γ will not lengthen the allowable timestep any further. Strong magnetic fields present in the DCFT cause the electron cyclotron frequency to dominate for most values of gamma used in this investigation.

Additionally, increasing the simulated Debye length allows the number of nodes required to represent a fixed domain size to decrease by a factor of γ^2. For statistical reasons, an increase in the simulated Debye length also allows the simulation to be run using γ^2 fewer particles for identical levels of statistical accuracy per cell.

Reducing the Mass of Heavy Species

Even with the effects of the permittivity factor γ, the time scales of heavy (neutrals and ions) and light (electrons) particles remain very different. In order to encourage the heavy particles to converge more quickly, the masses of all neutral and ionic species are reduced by the factor f, as shown in Equation 2.4. Simulated speeds of particles are now a factor of $\sqrt{f}$ larger than the actual value, for equivalent energies.

$$m^*_H \equiv \frac{m_H}{f}, \qquad f \geq 1 \tag{2.4}$$

Super-Particles

Finally, in order for the model to run within the constraint of available random access memory, super-particles are simulated, each one representing $\sim 10^8$ real particles in DCFT results presented here. Currently, ion and electron super-particles are equally weighted, though neutral super-particles are even larger. Ideally, this is done to bring the number of simulated particles for each species to the same order of magnitude. However, the drawback associated with increasing the size of super-particles is the loss of resolution that occurs when representing moments of the velocity distribution function. For instance, the smallest increment of density that can be simulated is a single particle per cell. Alternatively, simulated fluxes, such as the anode current or thrust, are subject to the same phenomenon within the simulation. The step size of a simulated flux value corresponds to one super-particle per time step. With such a strong magnetic field present in the DCFT, the combination of large super-particles and a time step dominated by the electron cyclotron frequency only adds to the statistical noise associated with quantities such as thrust, anode current and beam current.

Altering the mass and size of heavy species also changes simulated density and mean free path values. However, this is overcome by reducing the mass flow rate by a factor $\sqrt{f}$, while increasing collisional cross sections by the same factor. Additional details of this methodology are presented in Szabo's Ph.D. thesis[14], such as reducing the magnetic field seen by ions by the factor $\sqrt{f}$ to prevent ions from becoming falsely magnetized.

Chapter 3

DCFT Modeling Results

3.1 Boundary Conditions and Simulation Inputs

The first steps toward adapting the PIC model to the DCFT were to provide the vector magnetic field (Figure 3-3), structured mesh (Figure 3-2), and boundary types (Figure 3-1) as input files. The magnetic field was calculated using the Ansoft Maxwell software package, and then interpolated to the structured mesh. No significant differences between the calculated and interpolated magnetic fields have been observed, and the agreement between the simulated and measured magnetic field magnitudes along the centerline of the magnetic configuration has been demonstrated previously[2]. Figure 3-1 illustrates the different boundary types as classified by the PIC model. The area labeled as SIMULATION REGION represents the allowed locations of all particles in the simulation. The right hand side of the diagram shows the exit plane of the thruster. Future simulations would benefit from expanding this boundary further into the plume. The ANODE POTENTIAL represents all regions that have a constant potential equal to the applied voltage from anode to cathode, with the cathode assumed to be at zero potential. Explicitly modeling an external, off-axis cathode is not possible under the assumption of azimuthal symmetry. As a cathode surrogate, the upper-rightmost node of the simulation region is specified to be at cathode potential for all iterations. Additionally, electrons are injected at a temperature between 0.2 and 2.5 eV along cells on the righthand side boundary in order to prevent any deficit of electrons from developing.

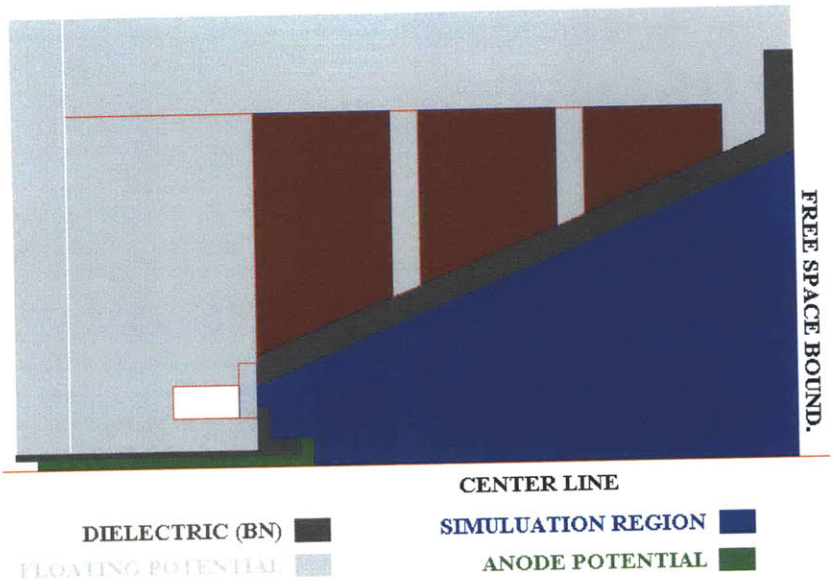

Figure 3-1: Boundary conditions used in the present investigation.

3.1.1 Grid Generation

The grid representing the simulation domain was made using an elliptic mesh generator created by Fife[12]. The node locations of the mesh shown in Figure 3-2 correspond to engineering models of the DCFT. The computational mesh should represent the physical domain as closely as possible, and the node spacing should be less than the modified electron Debye length (see Section 2.2.1) on the entire domain.

3.1.2 Calculating the Magnetic Field

The magnetic field was calculated using the Ansoft Maxwell software package, and then interpolated to the structured mesh. The result is shown in Figure 3-3. No significant differences between the calculated and interpolated magnetic fields have been noticed.

3.2 Collisions

Table 3.1 lists the types of collisions that are included in the model[14].

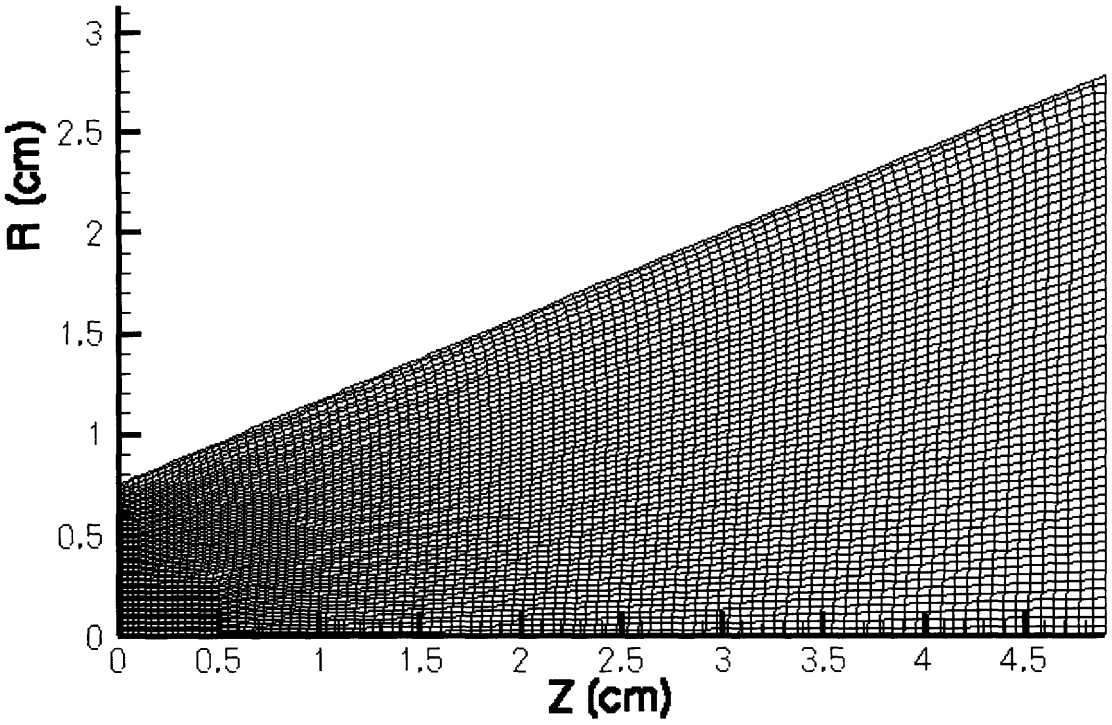

Figure 3-2: The 2 dimensional, structured, non-orthogonal, variable mesh used in these simulations.

Table 3.1: A listing of the collisions represented in the model. Some collision types that are not included are also provided.

Collision Types Included
(e^-)-(n) Elastic Scattering
(e^-)-(n) Ionization
(e^-)-(n) Excitation
(e^-)-(e^-) Coulomb
(e^-)-$(i^{+,++})$ Coulomb
$(i^{+,++})$-(n) Charge Exchange
$(i^{+,++})$-(n) Scattering
$(i^{+,++})$-(e^-) Wall Recombination
Collision Types Not Included
$(i^{+,++})$-$(i^{+,++})$ Coulomb
(n)-(n) Scattering
(e^-)-$(i^{+,++})$ Bulk Recombination

3.3 Coding Modifications

Changing the model to accurately simulate particle interactions with the new DCFT boundary conditions has been the most challenging aspect of this project. The most significant

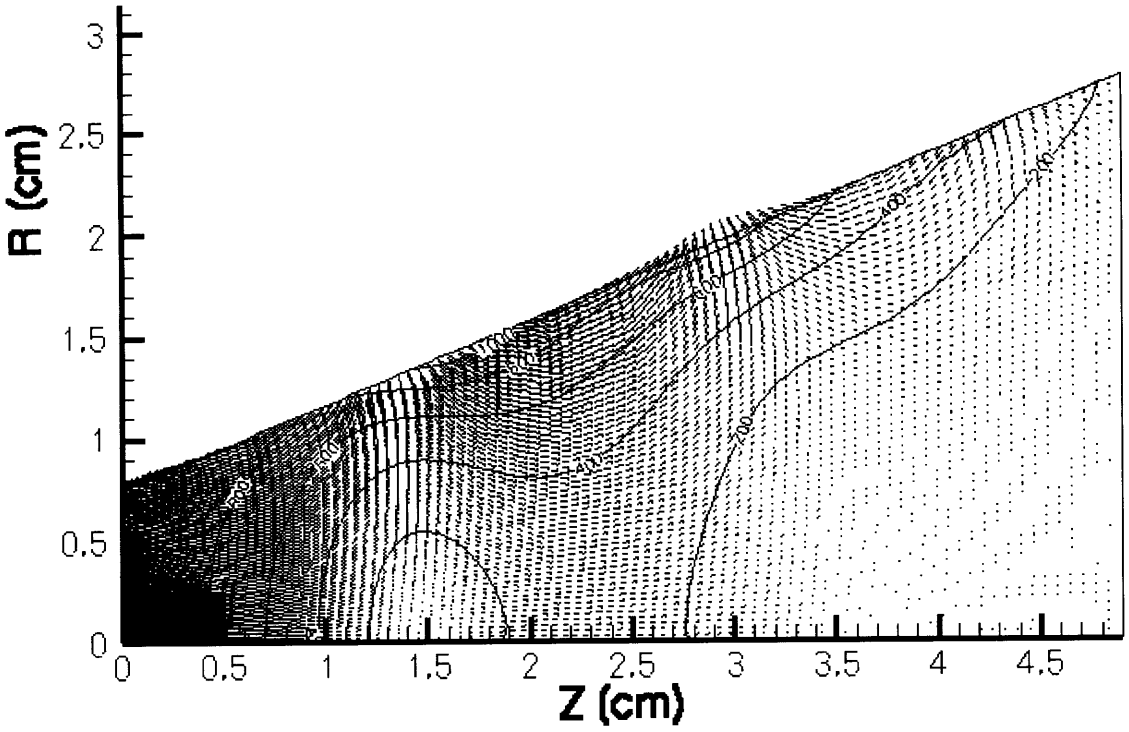

Figure 3-3: Magnetic field vector and magnitude for the simulation results shown in this paper. The actual magnetic field is a factor of 5 larger than shown. A simulated magnetic field was calculated using the Ansoft Maxwell software package[1, 2], and then interpolated to fit the computational mesh shown in Figure 3-2.

modifications include updating the logical structure of the code to include sloped walls, and tailoring the logical sheath method first implemented by Blateau[15] to the DCFT. To speed up execution time for cases when the electron cyclotron frequency determines the time step, a scheme is now executed that delays the poisson solver to run on the time scale of the maximum inverse electron plasma frequency, rather than during each iteration. The poisson solver represents a third to a half of the total computational cost per iteration, meaning that significant speedup of the model is obtained, and some of the original benefits associated with increasing the free space permittivity are recuperated. Finally, the method by which a plasma is originally seeded into the domain was varied to determine if the observed plasma structure was in fact a characteristic of the DCFT, or just an artifact of the initialization approach.

3.4 Simulation Results

The procedure for running a PIC simulation is as follows. First, a simulation is run with only neutral particles to allow an equilibrated neutral background on which to seed a plasma to develop. Next, electrons and singly charged ions are seeded throughout the domain at a specified temperature and density. From this point on, the particle trajectories are determined by the local Lorentz force, algorithms governing interactions with other particles and physical boundaries (ionization, wall recombination, collisions, reflection), and by the quench rule - with its roll in enhancing cross field diffusion above classical levels where appropriate. The collection of simulated particles evolves forward in time for a preset number of iterations, after which the results are analyzed. Although a fully kinetic simulation can never reach a truly steady state, the PIC model is said to have converged when characteristic simulated values obtain relatively constant values, or when outputs become periodic in nature. Quantities of interest for judging whether a simulation has converged or not include the total number of super-particles for each species present in the simulation domain, anode specific impulse, thrust, anode current and other flux related quantities.

3.4.1 Results with One-Fifth Magnetic Field Strength

Convergence

An important step toward creating a useful model of DCF thrusters is creating a model that converges. Reducing the magnetic field by a factor of 5 decreases the gyrofrequencies of all simulated particles by an identical factor, reducing the number of time steps required to simulate a given interval of time (i.e. the approximate neutral residence time)[1]. In this manner, a simulation of the DCFT was completed, providing convergent results for various performance variables and plasma characteristics. Unfortunately, the data presented here can not be directly compared to existing experimental results, though existing data may suggest the plausibility of the following results. The B/5 simulation was run with a xenon volumetric flow rate of 8.5 sccm and an applied potential difference from anode to cathode of 450 V. The mass factor value f=1000, and the permittivity factor γ=1200 were used. While the mass factor is of the same order as values used in previous works, the permittivity factor

[1] Assuming the electron gyrofrequency remains larger than the modified electron plasma frequency. Modifying the electron plasma frequency is done by artificially increasing the permittivity of free space. See Section 2.2.1.

is much larger than has been used for past studies at the MIT SPL. The super-particle size for electrons and ions was 1.3×10^8, while neutral particles began the simulation 50 times larger than charged particles.

Figures 3-5(a), 3-5(b), 3-6(a), 3-6(b) and 3-6(c) all suggest convergence of the DCFT model. Unfortunately, no such convergence has been obtained for a simulation incorporating the full magnetic field strength present in a real DCF thruster. The simplest explanation is that the simulation has not been allowed to run for a sufficient number of iterations, though full strength B cases have shown divergent characteristics less than half way through attempts to run the model for a million iterations or more. Another possibility is that during the strong transient behavior exhibited by the converged simulation during the first 250,000 to 300,000 iterations (as seen in Figures 3-5(a) and 3-5(b)) the simulation diverges due to high plasma densities (corresponding to very large numbers of super-particles). This would occur if local Debye lengths were to fall below the characteristic length of a given cell for a prolonged number of iterations. It is possible that this instability is initiated within one portion of the grid, and then spreads to surrounding cells. In fact, this behavior was observed to arise in the upper right corner of the anode, even in the B/5 case, which led to simulations being run with γ=1200, rather than with $\gamma \leq 100$ as before. Conceivably, the full B case exacerbates the problem in which the local Debye length falls well below the resident cell size, leading to instabilities which cause the simulation to diverge after several tens of thousands of iterations. All the results shown in the next section correspond to a simulation run with the magnetic field reduced to 1/5 its actual value.

Figures 3-5(a) and 3-5(b) show how the total number of super-particles for each species changes over the course of the entire simulation. After 300,000 iterations, the number of super-particles for each species levels off, indicating that the simulation has converged. Also significant is the fact that after about the $250{,}000^{th}$ iteration, the total numbers of electron and ion super-particles are within 10% of each other, indicating that the simulation domain is nearly globally neutral. The slight excess of electron super-particles can be explained by the fact that, while ions can only enter the simulation domain as a result of ionization events, electrons have the additional source of the righthand-side boundary, where electrons are injected to implicitly simulate the presence of a cathode. Another explanation could be that the ion super-particle population includes a number of doubly charged ions, requiring a fewer number of simulated ions compared to simulated electrons.

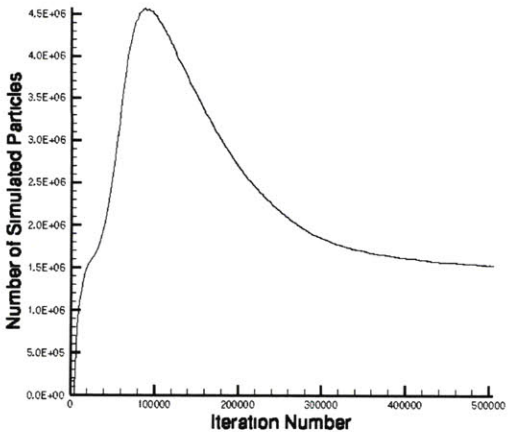

(a) The number of neutral species super-particles for each iteration.

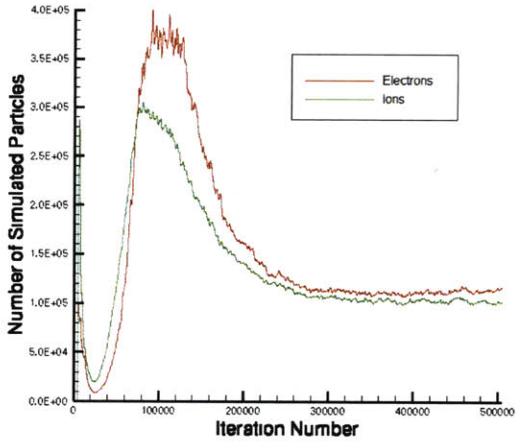

(b) The number of charged species super-particles for each iteration. The count of ion super-particles includes doubly and singly charged ions.

Figure 3-4: The number of super-particles representing each species of particle is plotted for each iteration of the simulation.

Super-particle Distribution

Figures 3-5(a) and 3-5(b) show the distribution of super-particles for electrons and ions as the number of super-particles per cell. As expected, electron super-particle densities are the greatest within the magnetic cusps. As a result, the values of simulated electron macroscopic quantities such as density, temperature and velocity are relatively insensitive to the flux of a small number of particles into or out of cells within the cusps. Contrastingly, the values of such quantities in regions outside the cusps can be expected to exhibit stronger statistical fluctuations about a mean value. Less obvious is the presence of a large group of simulated electrons just above the anode. Apparently, a strong electric field, arising from the sharp corner of the downstream anode face, results in the creation of a very dense plasma. This feature is present in many results presented here.

Simulated ions are are much more spread out than the electrons. As will be addressed when Figures 3-12(a) and 3-12(b) are presented, the computational grid used here limits the value of the permittivity factor (γ) to a minimum value of around 1200. Thus, the strong internal electric fields that would normally maintain local charge neutrality are lessened as γ increases.

Performance Variables

Figure 3-6(a) illustrates that the anode specific impulse of the modeled DCFT converges to a value of approximately 1500 s, or within 8% of the value measured experimentally (1400 s) for the same operating flow rate and anode potential[1]. Although making comparisons between experimental data and simulated data for the same thruster with different magnetic field strengths is not ideal, it is the only rubric by which the simulated results can be measured. As such, they should not be taken absolutely. However, this result suggests that a converged simulation for the full strength magnetic field case should be able to predict specific impulse to within a reasonable margin. According to Figure 3-6(b), the average total simulated thrust is $\approx$14 mN, the beam current is $\approx$.6 A, the anode current is $\approx$1 A, and the neutral current (corresponding to the current that would result from singly ionizing all incoming propellent) is 0.61 A. Thus, according to Equations 3.1, 3.2 and 3.3, $\eta_t = 26\%$, $\eta_b = 60\%$ and $\eta_u = 98\%$.

$$\eta_t = \frac{T^2}{2\dot{m}_a P_a} \tag{3.1}$$

$$\eta_b = \frac{I_b}{I_a} \tag{3.2}$$

$$\eta_u = \frac{I_b}{I_n} \tag{3.3}$$

The anode thrust, beam and utilization efficiencies could be interpreted to mean, that at 1/5 B, the DCFT is operating in the high current mode characterized in existing DCFT references[1, 6, 2]. This is supported by Figure 3-7(a), which shows two distinct regions of relatively high temperature electrons between the anode and the upstream cusp, and again between the two cusps. The high utilization efficiency is probably due to the fact that the weak magnetic field allows the ionization region to spread closer to the walls than otherwise, allowing a greater portion of the flow to be ionized. In addition, doubly charged ions could be contributing to the high utilization efficiency determined by the model. Another symptom of the weaker magnetic field is the low anode thrust efficiency and beam efficiency. The 1/5 magnetic field reduction increases electron mobility to the anode by weakening the magnetic bottle system that would normally be in place. The result is a larger anode current, reducing the beam efficiency and increasing the power consumed by pumping electrons from anode to cathode.

Plasma Structure

The ion velocity vectors as visualized in Figures 3-8(a), 3-8(b) and 3-8(c) suggest that the magnetic field has a strong influence on ion trajectories. Figure 3-8(c) shows bulk azimuthal ion speeds increasing near the walls, which are the areas closest to the strongest magnetic fields. The directions of bulk ion speeds in the azimuthal direction are consistent with grad-B and curvature drifts. Furthermore, the upstream cusp has a more distinct effect on ion velocities than the downstream cusp, especially as seen in Figure 3-8(a). For both cusps, the ions are seen to obtain a maximum axial speed just before entering the cusp, and then emerge from the cusped-field region with a speed lower than they entered with. Unpublished measurements of ion velocities using laser-induced fluorescence on a CHT reveal azimuthal ion speeds with magnitudes of the same order as shown in Figure 3-8(c)(Hargus, W.A., personal communication, July 23, 2009). An examination of ions and their velocities outside the chamber is not possible due to the location of the downstream mesh boundary. When interpreting these or any plots in this section, it is important to keep in mind that these are snapshots of a kinetic simulation, and so these values do not necessarily represent time averaged quantities very accurately. From Figures ?? and ??, these fluctuations will be lower within regions with larger numbers of simulated particles per cell. Also, the imposed boundary conditions on the righthand-side boundary may be altering the ion trajectories in a manner that is not physical. The artificial nature of the exit plane boundary conditions should be considered when interpreting these data.

Figures 3-9(a), 3-9(b) and 3-9(c) show the axial, radial and azimuthal macroscopic electron velocity magnitudes, respectively. The axial speed distribution shows the electron velocities slowing within each cusp on their way upstream toward the anode. Figure 3-9(b) predicts that the only locations where the bulk flow is traveling toward the divergent, insulating wall are within the cusps and just above the anode. Azimuthally, the direction of electron velocities do not appear to be consistent with ExB drifts seen in Hall thrusters. In Section 4.1.1, an attempt to account for the direction and magnitude of polar electron velocity is made.

Figures 3-10(a), 3-10(b), 3-11(a) and 3-11(b) were calculated from simulation results at the $350{,}000^{th}$ iteration according to Equations 3.4 and 3.5. These equations hold if only hydrostatic pressure terms are considered to contribute to the mean squared random ve-

locity magnitude. The parallel and perpendicular directions are defined relative the local direction of the magnetic field. The electron temperature plots demonstrate that the electron temperatures in the parallel and perpendicular directions are very similar in value, suggesting that random electron energy distributions are nearly isotropic with respect to magnetic field lines. The same cannot be said of ions, however, as their temperature within the cusps is nearly entirely perpendicular to the magnetic field, while between cusps, the ion temperature is nearly all parallel to magnetic field lines.

$$T_{\parallel} \approx T_z \left(\frac{B_z}{B}\right)^2 + T_R \left(\frac{B_R}{B}\right)^2 \tag{3.4}$$

$$T_{\perp} \approx \frac{1}{2}\left[T_\theta + T_z \left(\frac{B_R}{B}\right)^2 + T_R \left(\frac{B_z}{B}\right)^2\right] \tag{3.5}$$

Figures 3-12(a) and 3-12(b) show an instantaneous view of the electron and ion number density distributions for the $350{,}000^{th}$ iteration. This iteration number was chosen because it is representative of values that can be expected after the simulation was observed to converge. Figures 3-13(a) and 3-7(a) are also snapshots of the respective spatially varying variables at the $350{,}000^{th}$ iteration. Apparent regions lacking charge neutrality can be explained by the fact that electrostatic forces have been reduced by a factor γ^2, where $\gamma = 1200$ in this case. However, the boundary potentials of the anode and cathode are enforced, meaning that as the permittivity factor $\gamma \rightarrow \infty$, the potential distribution that results from solving Poisson's equation is replaced by a linear potential distribution associated with Laplace's equation, as shown in Equation 3.6.

$$\lim_{\gamma\to\infty} \nabla^2\phi = \lim_{\gamma\to\infty} -\frac{\rho_{charge}}{\epsilon_o \gamma^2} = 0 \tag{3.6}$$

From examining Figure 3.4.1, it seems likely that the neutral injector floating boundary is initialized to a zero potential and then remains at that potential for the duration of the simulation. This will be addressed in future simulations. Figure 3-12(a) very clearly illustrates the fact that electrons are effectively bottled in and between the cusps. The high electron density in the cusps is to be expected, due to the fact that electron guiding centers are slowed as they approach the ceramic wall. Therefore, the electron density should increase. Conversely, as the electrons follow the magnetic field lines out of the cusps, into

regions with weaker magnetic fields, their velocity parallel to the magnetic field increases as the tradeoff necessary to maintain the invariant value of the average magnetic moment for each electron occurs.

The components of the simulated electric field vectors are plotted in Figures 3-14(a) and 3-14(b). The electric field structure within the cusps appears to change sign in the radial and axial directions.

Time Resolved Analysis

Time resolved anode current measurements show that DCFT operation is characterized by low frequency oscillations on the order of 3 or 4 kHz[22]. As such, the period of such an oscillation is on the order of 250 μs. The total time elapsed for the simulated data presented here is only about 24 μs, which is not a sufficient amount of time over which to expect time resolved currents to be reproduced, especially if you consider the percentage of the simulated time the thruster required to converge to a performance regime (see Figure 3-5(b)).

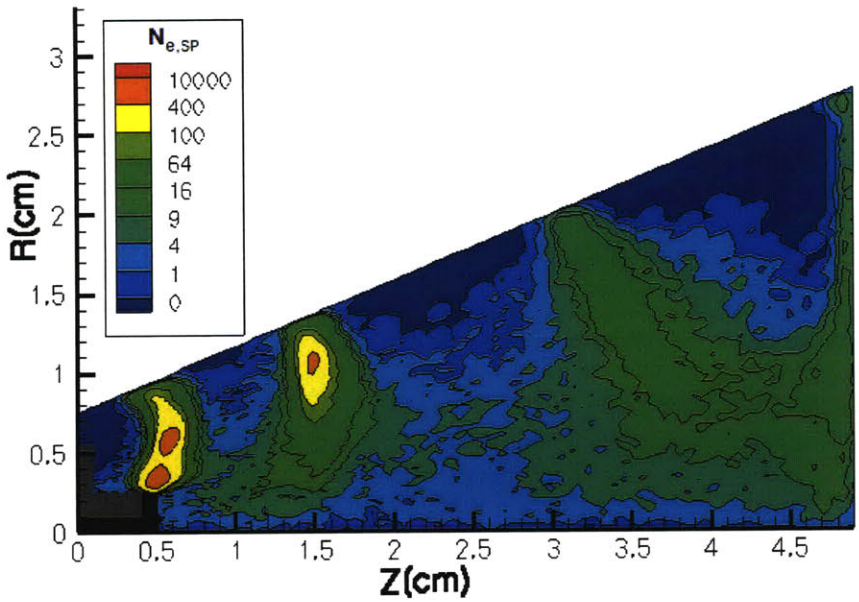

(a) The number of electron super-particles per cell.

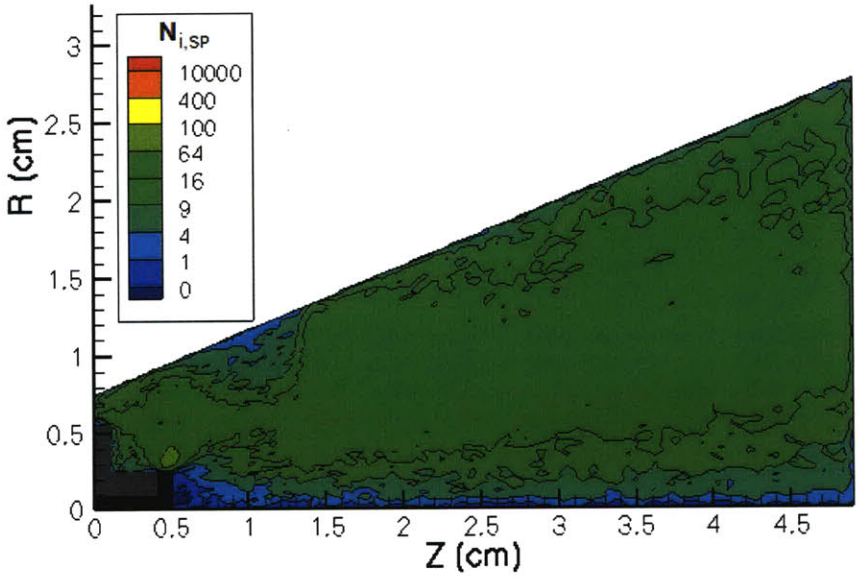

(b) The number of ion super-particles per cell. The counts shown here include singly and doubly charged ions.

Figure 3-5: The spatial variation of the concentration of simulated particles per cell at the $350{,}000^{th}$ iteration. The statistical noise associated with moments of the velocity distribution function in a given cell is proportional to the inverse of the square root of the number of particles occupying that cell. Thus, a cell containing only 4 particles would have about 4 times as much noise as a cell containing 64 particles (i.e. a standard deviation 4 times larger).

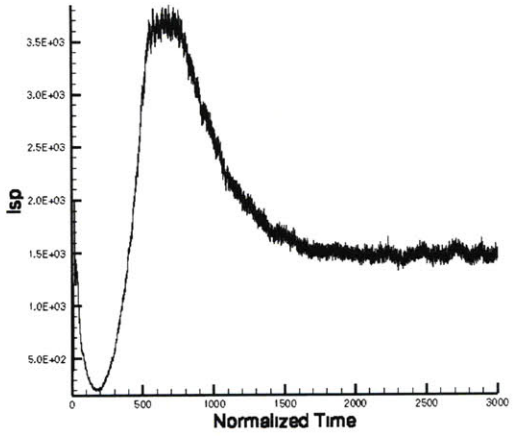

(a) Anode specific impulse at each instant of time.

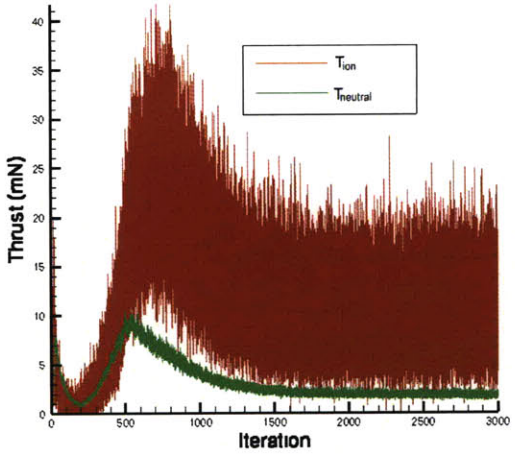

(b) Thrust at each instant of time. The large amount of statistical noise apparent here is due to the size of the ion super-particles. As the super-particle size increases, the resolution of any particle flux deteriorates, for a fixed velocity magnitude.

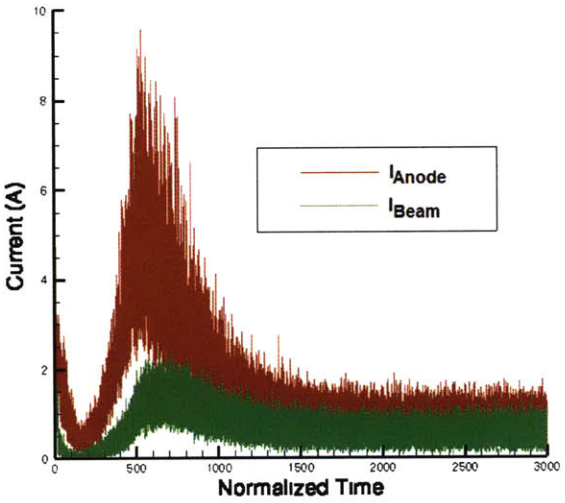

(c) Anode and beam currents plotted at each instant of time.

Figure 3-6: Performance variables plotted as a function of normalized time. For the present simulation, one unit of time is 8.0 ns.

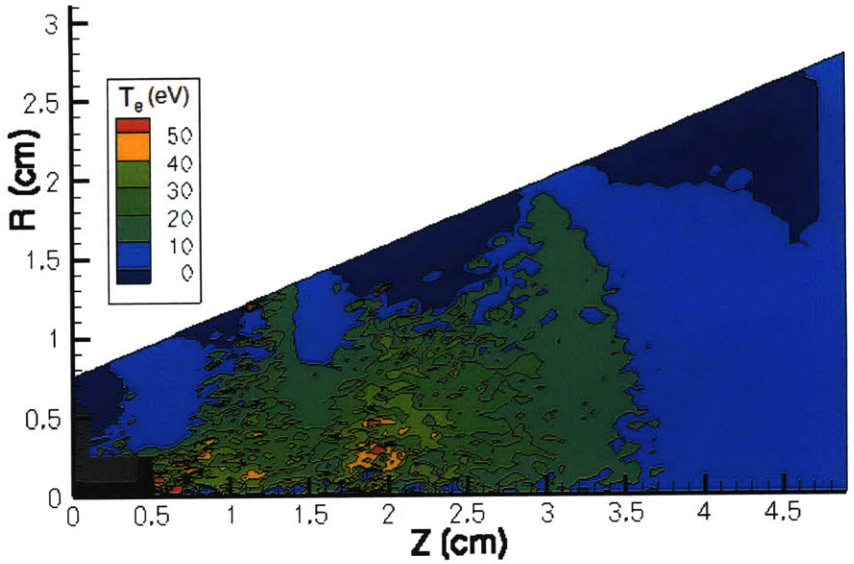

(a) Instantaneous electron temperature distribution at the 350,000th iteration.

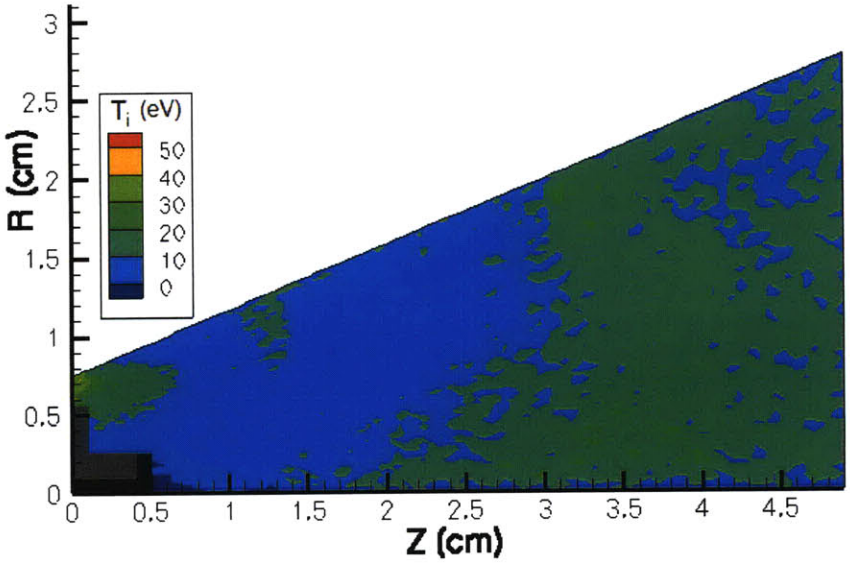

(b) Instantaneous ion temperature distribution at the 350,000th iteration.

Figure 3-7: Electron and ion temperature.

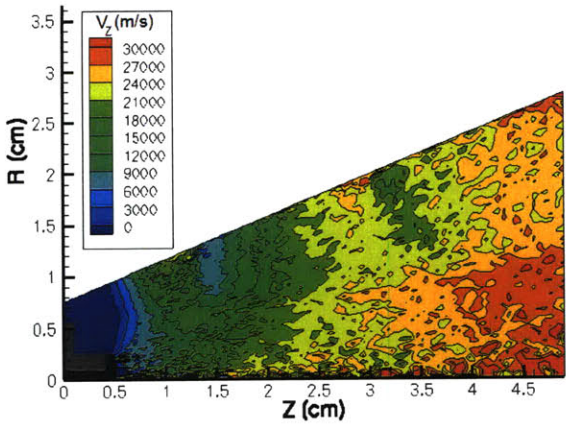

(a) Ion axial speed.

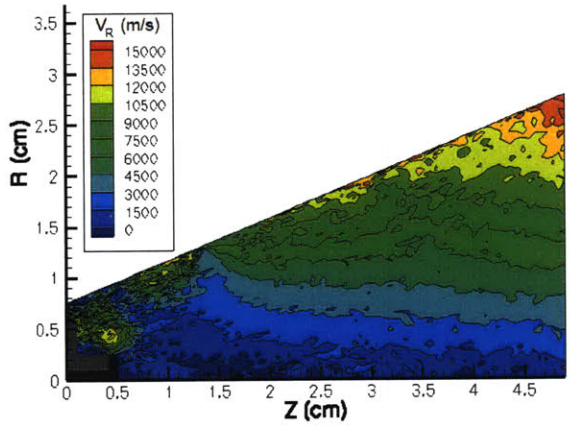

(b) Ion radial speed.

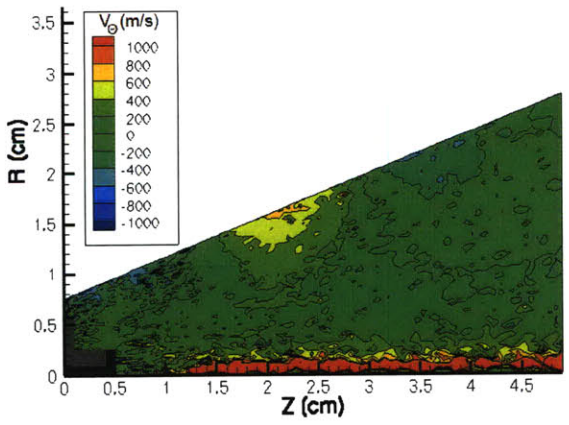

(c) Ion azimuthal speed.

Figure 3-8: Ion speeds in all three dimensions are plotted for the 350,000th iteration.

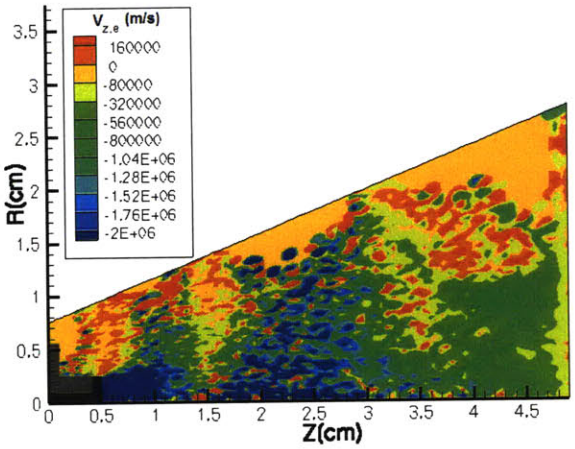

(a) Electron axial speed.

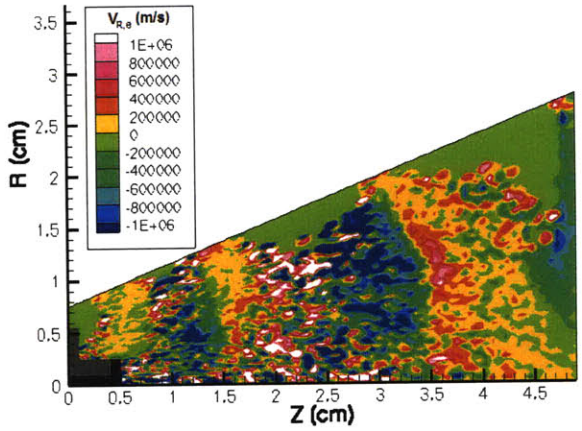

(b) Electron radial speed.

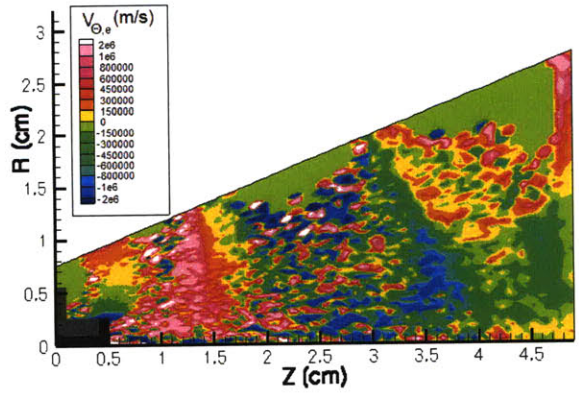

(c) Electron azimuthal speed.

Figure 3-9: Electron speeds in all three dimensions are plotted for the 350,000th iteration.

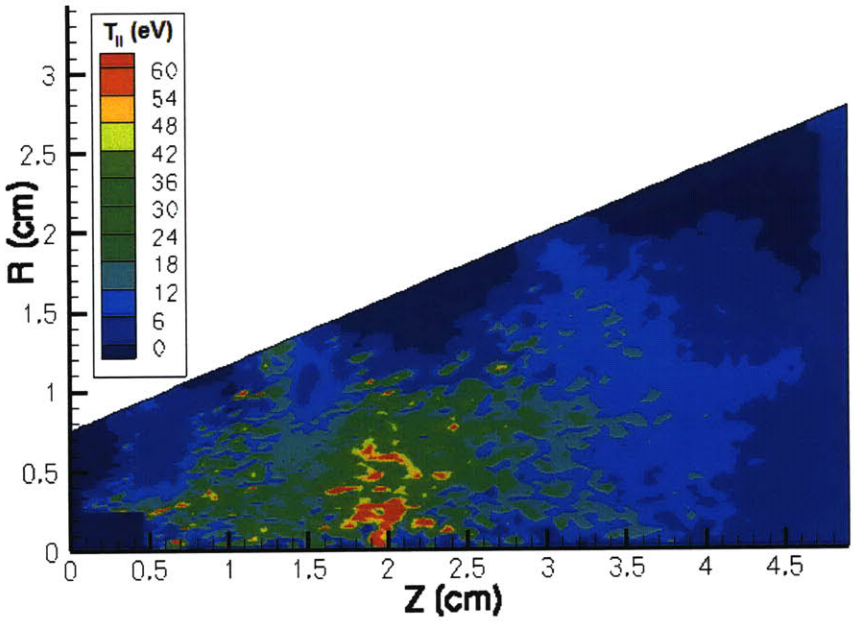

(a) Instantaneous electron temperature, parallel to the magnetic field lines.

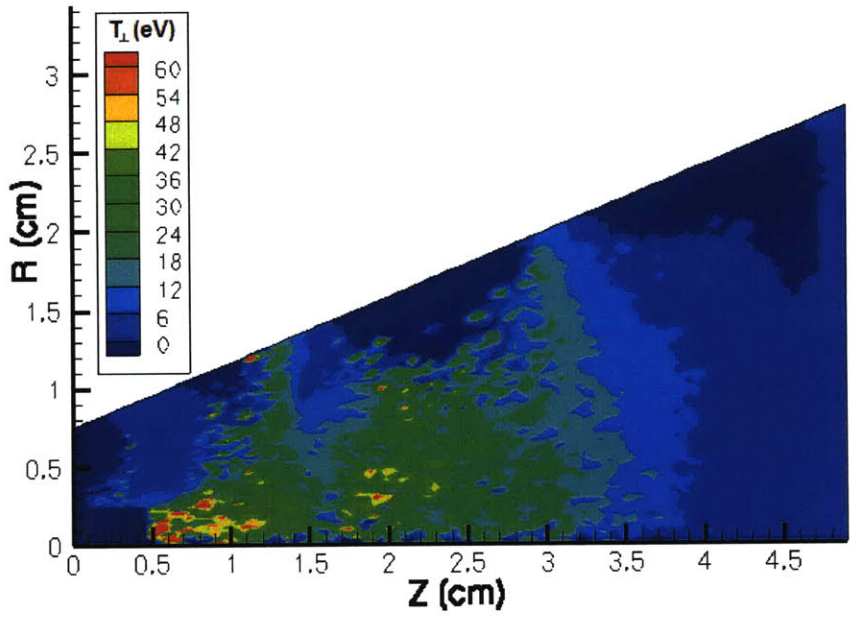

(b) Instantaneous electron temperature, perpendicular to the magnetic field lines.

Figure 3-10: Electron temperature with respect to magnetic field directionality.

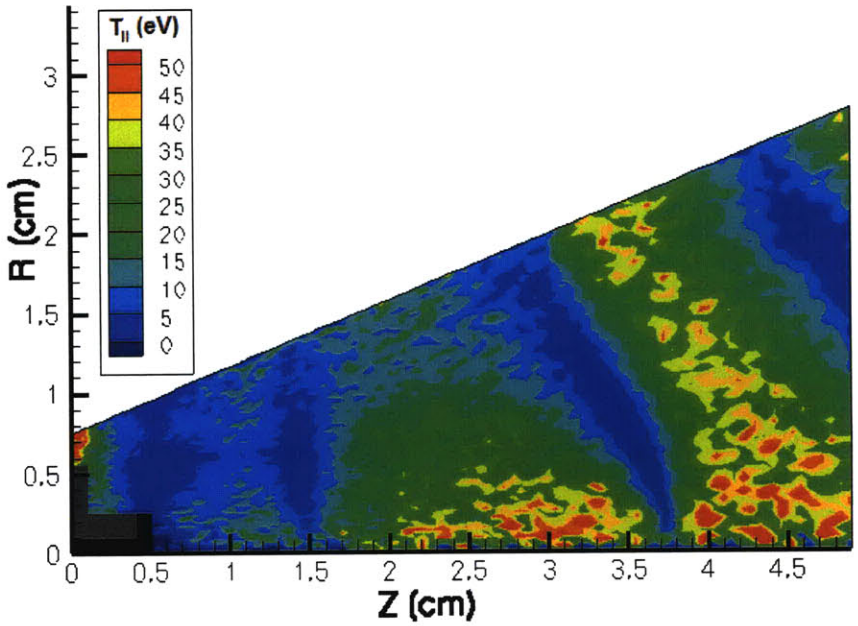

(a) Instantaneous ion temperature, parallel to the magnetic field lines.

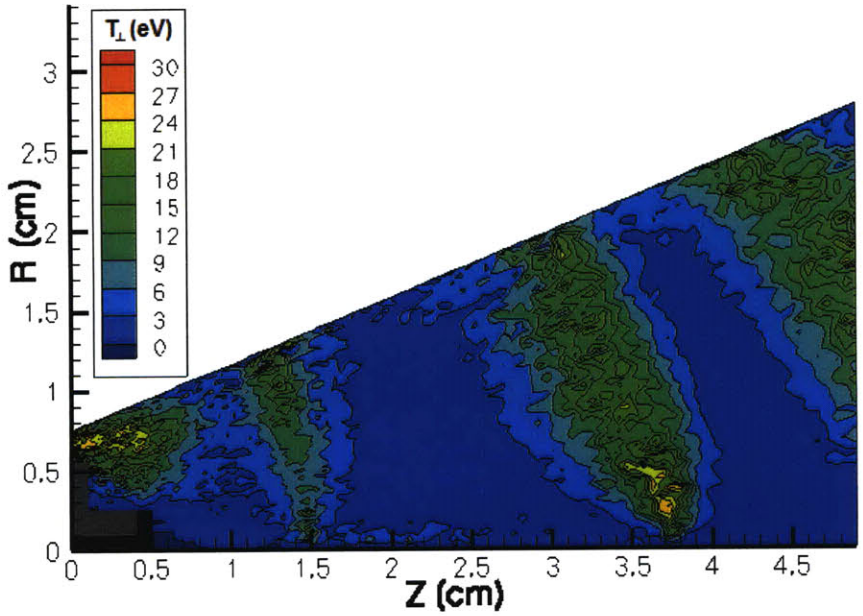

(b) Instantaneous ion temperature, perpendicular to the magnetic field lines.

Figure 3-11: Ion temperature with respect to magnetic field directionality.

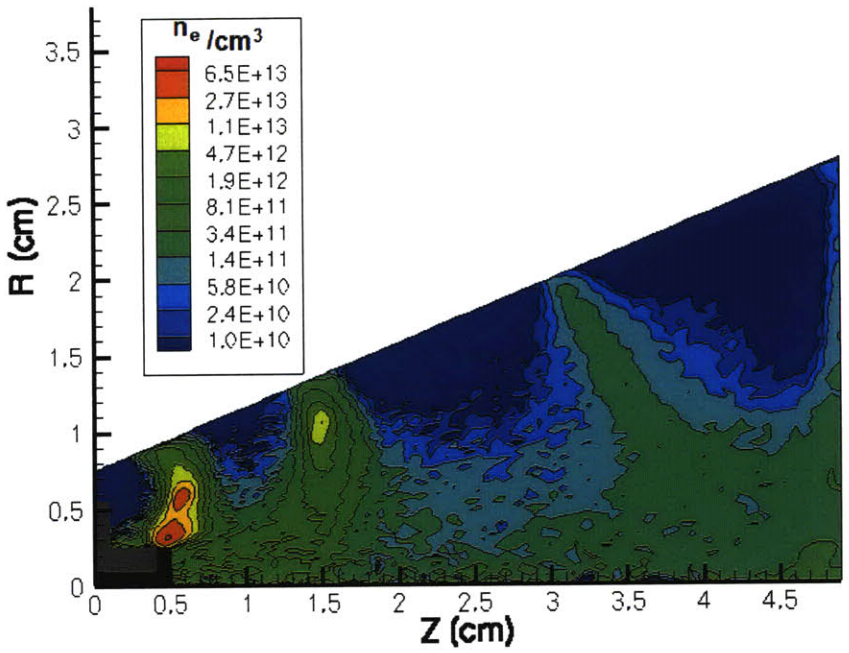

(a) Instantaneous electron number density.

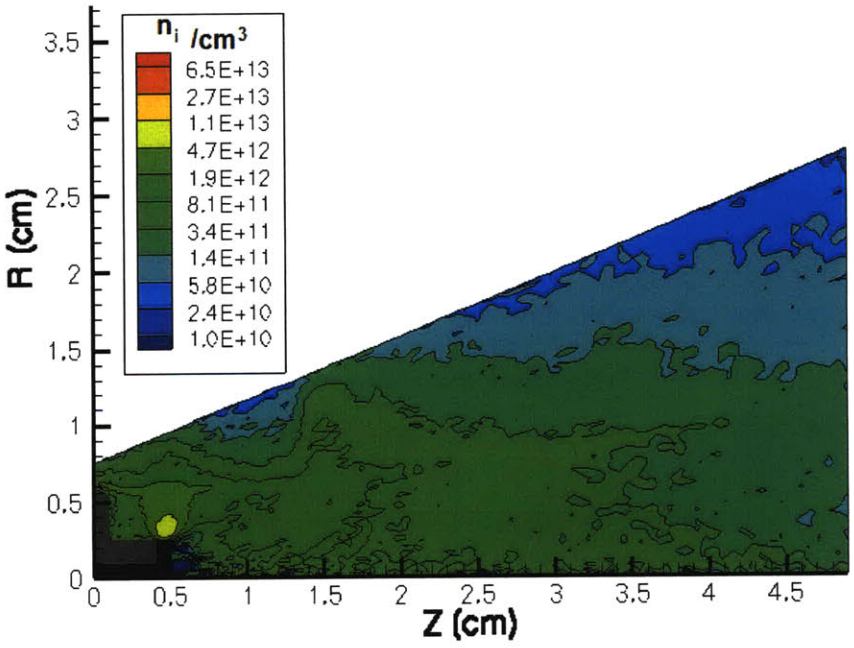

(b) Instantaneous singly charged ion number density.

Figure 3-12: Electron and ion number densities.

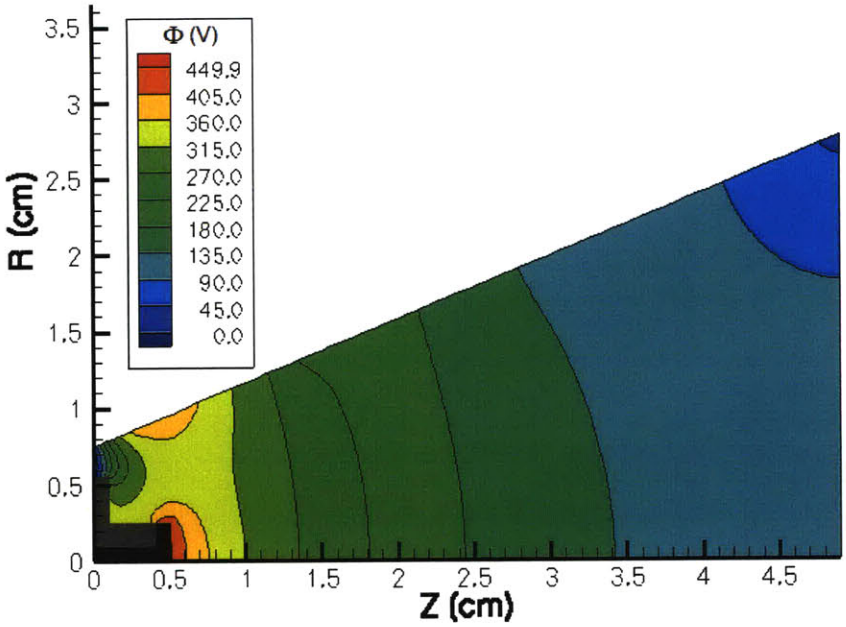

(a) DCFT instantaneous potential distribution for the 350,000th iteration, with plasma present.

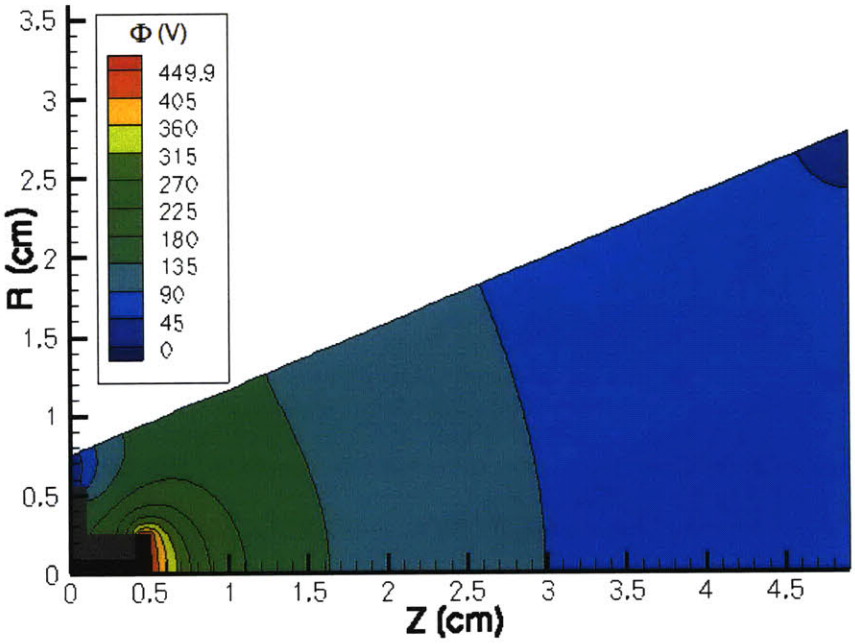

(b) Vacuum potential of DCFT. This potential distribution is present during the neutrals only simulation referenced in Section 3.4.

Figure 3-13: The instantaneous potential distributions with and without plasma present in the DCFT chamber.

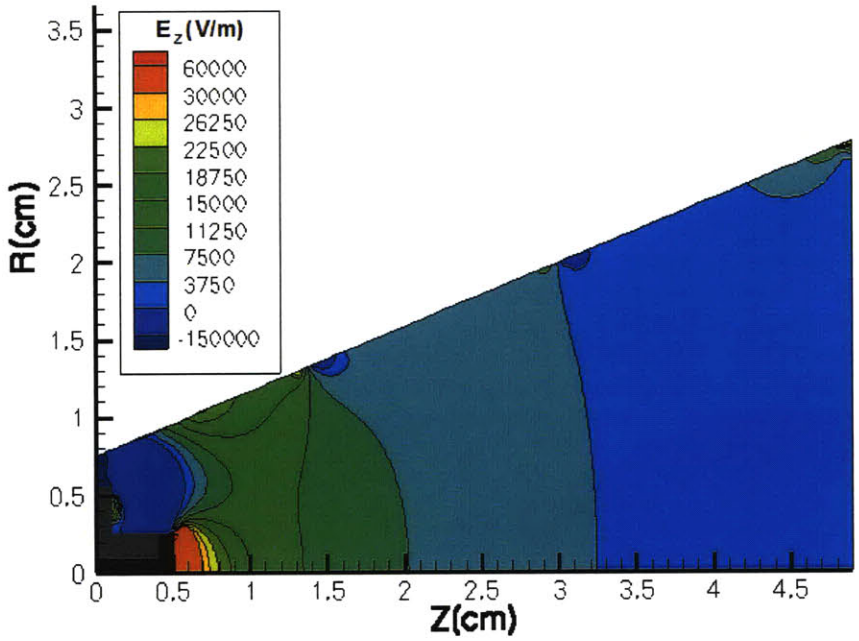

(a) The axial component of the electric field.

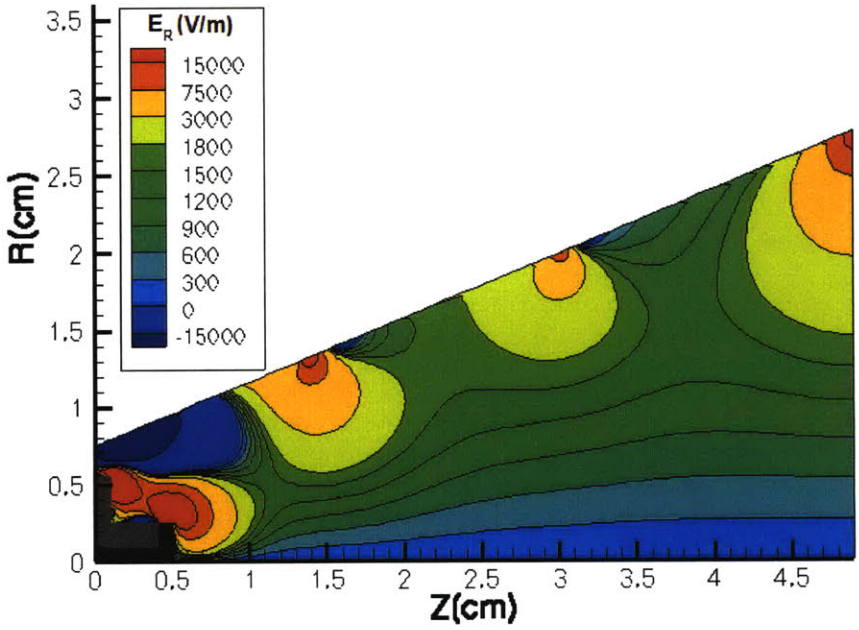

(b) The radial component of the electric field.

Figure 3-14: The gradient of the scalar potential from Figure 3-13(a), for the 350,000th iteration.

Chapter 4

Conclusions and Future Work

Simulations of the performance and plasma dynamics of the DCFT were unable to be completed for the case of full magnetic field strength (B). However, reducing B by a factor of 5 allowed a convergent simulation to be run, which is an important intermediate step toward simulating a real DCFT. Although the results presented here indicate that anode specific impulse and thrust would not change by more than a few tens of a percent as a result of the weakened magnetic field, the anode thrust efficiency would drop by nearly 50%. Weakening the magnetic field by a factor of 5 increases the mobility of electrons to the point that the anode current could be expected to double. As simulated, the DCFT was running in the high current mode, characterized by the presence of two distinct ionization zones; one located between the anode and the upstream cusp, and the other located between the two cusps[1]. Furthermore, insights into the basic operating principles are possible by examining the trajectories of ions and electrons within the DCFT chamber.

4.1 DCFT Operating Principles

In order to understand the basic operating principles of the DCF thruster, it will be important to determine the roll that azimuthal currents play in determining the performance of cusped-field thrusters. To reach this task, it will be beneficial to establish what kinds of currents are present and what their causes are. The most obvious candidates are guiding center drifts that arise when real or effective forces are applied to charged particles moving through magnetic fields. Identifying candidate drift phenomena, as well as determining where a species is magnetized, will allow insight into which drift velocities are the most

significant within a given region of the thruster.

4.1.1 Electron and Ion Drift Velocities

Hall effect thrusters take their name from the Hall current, an azimuthal electron current that arises as magnetized electrons move under the combined influence axial electric and radial magnetic fields. Their guiding center drift velocity is given by Equation 4.1, and plotted for the DCFT simulated at 1/5 magnetic field strength in Figure 4-1(a). The direction of the drift does not depend on the charge of particle, and hence, if both species are magnetized within a given region, no net current is established. Therefore, the lack of magnetized ions is essential to the operation of Hall effect thruster.

$$\vec{v}_{E\times B} = \frac{\vec{E}\times\vec{B}}{B^2} \tag{4.1}$$

Although lacking prevalence in Hall thrusters, the drifts related to magnetic field topology can also give rise to currents within plasmas. Unlike the Hall current, these drifts, referred to as gradient-curvature drifts, drive currents even when ions and electrons are both magnetized[23]. However, the magnetization current that arises due to nonuniformities in the magnetization of a plasma often have a canceling effect on current densities arising from gradient-curvature drifts(Martínez-Sánchez, M., personal communication, August, 2009). A simple demonstration comes from drawing a current through a long straight wire surrounded by a plasma. The currents that would occur based solely on gradient-curvature drifts are canceled out exactly by the magnetization current, given in Equation 4.3. Therefore, devices like the DCFT, having magnetic field strengths much larger in magnitude than Hall thrusters of similar size, could conceivably operate by some mechanism other than the Hall effect. In fact, the regions within the thruster chamber where ions are magnetized will determine where it is not possible for Hall currents to establish themselves.

$$\vec{v}_{GC} = \frac{1}{q}\left(KE_{\parallel} + \frac{1}{2}KE_{\perp}\right)\frac{\vec{B}\times\nabla\left(B^2\right)}{B^4} \tag{4.2}$$

$$\vec{j}_{M,s} = \nabla\times\vec{M}, \quad \vec{M} = -\left(\frac{n_s KE_{\perp,s}}{B^2}\right)\vec{B} \tag{4.3}$$

The azimuthal velocities for ions and electrons shown in Figures 3-8(c) and Figures 3-9(c) show the direction changing before and after each magnetic cusp. For electrons, this change

is observed over the entire radial distance of the thruster near the upstream and downstream cusps. The ions, however, exhibit the change in direction of the azimuthal velocity much closer to the chamber walls, where the magnetic field is strongest. This suggests that the ions are indeed magnetized within the DCFT.

Comparing the structure of the azimuthal velocities of ions and electrons with Figures 4-1(a) and 4-1(b), only the gradient-curvature drift velocity can account for the structure and direction of ions and electrons in the cusps based the simulated data generated in this study. However, upstream cusp nearest to the anode (z ¡ 1 cm), the ExB drift provides a more similar picture of the azimuthal electron current density distribution, shown in Figure 4-2. Although evidence suggests that ions are magnetized within some regions of the DCFT, there contribution to the azimuthal current density is negligible compared to the electron current in the same direction. Noticing that the ExB and gradient-curvature magnitudes are both proportional to 1/B, the magnitude of the azimuthal velocity of ions and electrons will be lower in the actual DCFT as compared to the magnetic field simulated here.

4.1.2 Ion and Electron Magnetization

Figure 4-3 corroborates results presented in Figure 3-8(c) suggesting that ions are magnetized within the DCFT. In fact, this study has shown that, even with 1/5 the magnetic field actually present in the design studied here, a significant portion of the DCFT ion population is magnetized. The degree of magnetization in the full field DCFT should be higher than the case simulated here. The values of the ion Hall parameter (Ω_i) presented in Figure 4-3 were calculated by determining the ion cyclotron frequency based on the magnetic field data file used as input to this simulation, and by estimating the value of the ion collisional frequency($\nu_{c,i}$). The magnetization profile visible in Figure 4-3 may explain the hollow distribution of energetic ions within the plume, as measured previously[6].

The ion collision frequency can be estimated by determining the cross sections for various types of collisions, and then calculating the contribution from each collision type individually. Following the method used by Szabo, the collisions included in this estimate of the total ion momentum transfer frequency are ion-neutral charge exchange, ion-neutral elastic scattering, and ion-electron coulomb interactions[14]. The cross section for each type of

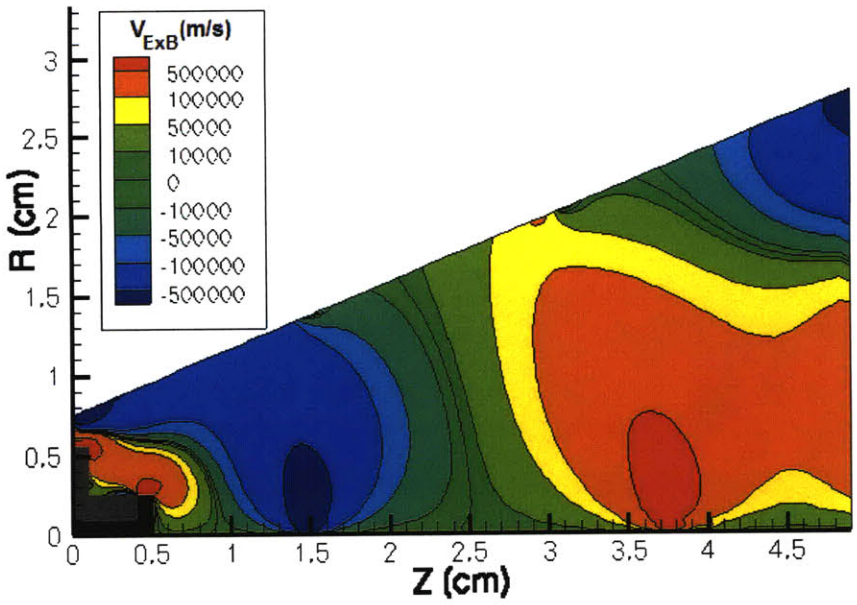

(a) Calculated ExB drift velocity magnitude. The electric and magnetic fields are assumed to have no azimuthal components. The ExB drift speeds were determined by calculating the cross product of the electric field shown in Figures 3-14(a) and 3-14(b) with the static magnetic field shown in Figure 3-3

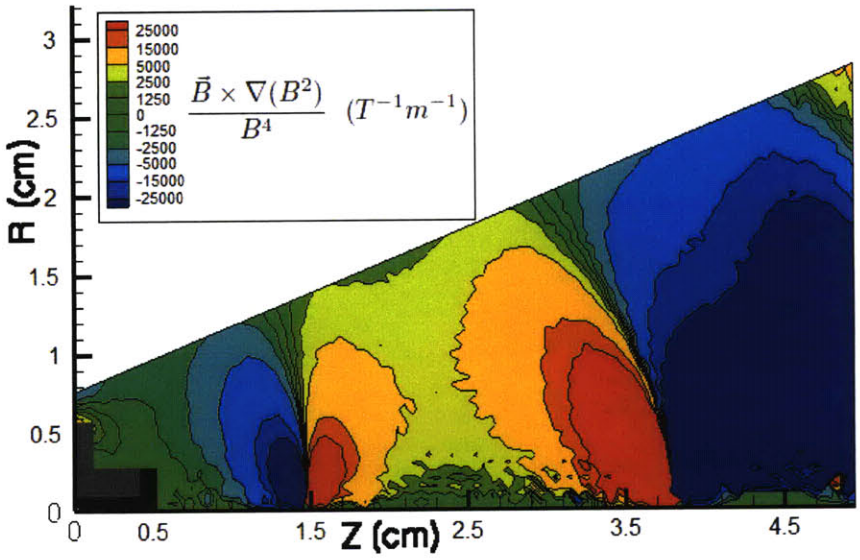

(b) The gradient-curvature drift is proportional to the quantity plotted here. The complete expression is provided in Equation 4.2.

Figure 4-1: Calculated azimuthal velocities for ExB drifts, and the variation of the term depending on magnetic topology in the gradient-curvature drift.

collision are given in Equations 4.4, 4.5 and 4.6.

$$Q_{cex} = [-.8821 \ln c_r + 15.1262]^2 \times 10^{-16} \ \ cm^2, \ c_r \ expressed \ in \ m/s \tag{4.4}$$

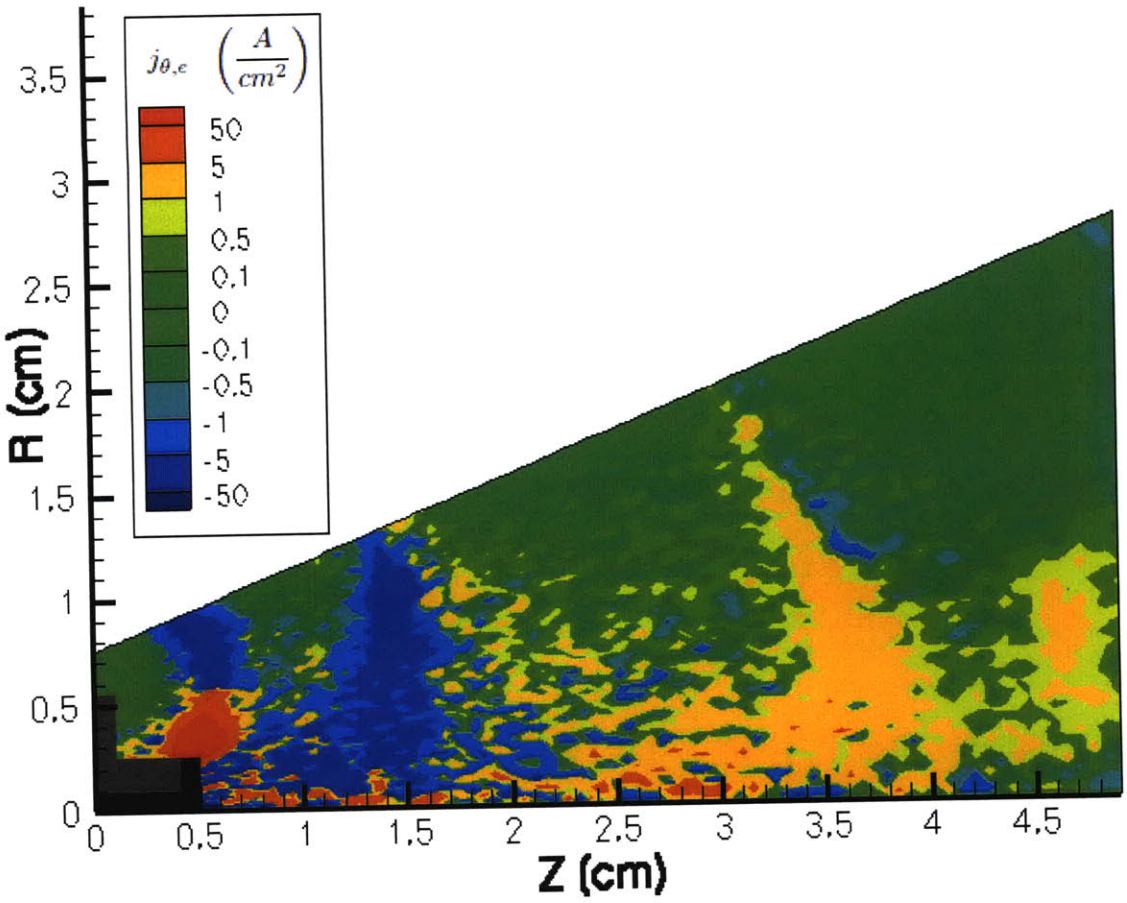

Figure 4-2: Azimuthal current density, calculated from quantities shown previously in Figures 3-9(c) and 3-12(a).

$$Q_{es} = \frac{8.28072 \times 10^{-10}}{c_r} \ cm^2, \ c_r \ expressed \ in \ cm/s \tag{4.5}$$

$$Q_c = \frac{6.5 \times 10^{-14} \ln \Lambda}{E^2} \ cm^2, \ E \ expressed \ in \ eV \tag{4.6}$$

The ion-neutral charge exchange(Q_{cex}), ion-neutral elastic scattering (Q_{es}), and ion-electron coulomb (Q_c) cross sections were then combined with Equation 4.7 to complete the calculation of the ion collision frequency. In Equations 4.4 and 4.5, c_r was assumed to be the ion thermal speed, $\sqrt{\frac{kT_e}{m_i}}$. In Equation 4.6, E is approximated as the average relative energy of electrons with respect to ions, whose energy can be neglected: $\left(\frac{3}{2}kT_e\right)$

$$\nu_{c,i} = n_e Q_c \bar{v}_{i,e} + n_n \left(Q_c ex + Q_e s\right) \bar{v}_{i,n} \tag{4.7}$$

In Equation 4.7, $\bar{v}_{i,e}$ is assumed to be the mean electron thermal speed for a Maxwellian

distribution $\sqrt{(\frac{8kT_e}{\pi m_e})}$, and $\bar{v}_{i,n}$ is assumed to be the ion sonic speed, $\sqrt{(\frac{kT_e}{\pi m_i})}$

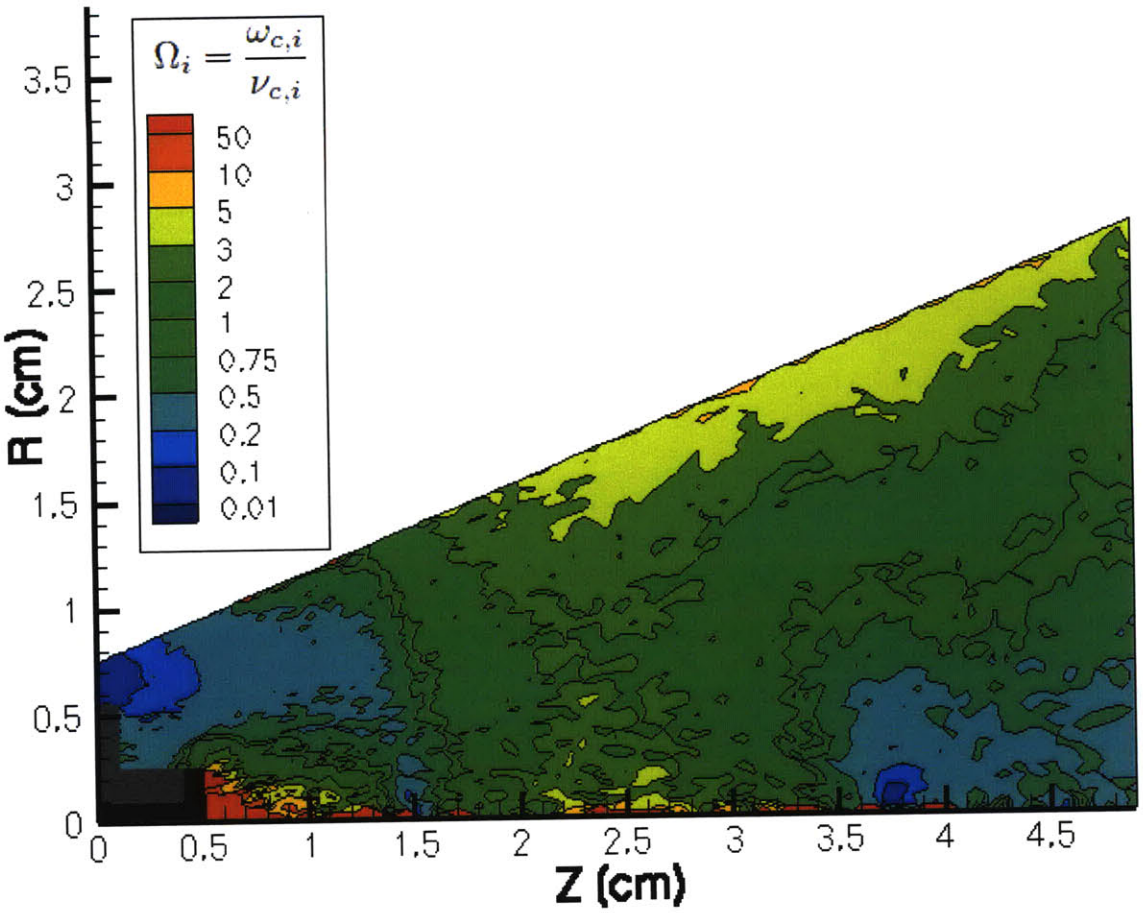

Figure 4-3: DCFT Ion Magnetization Assessment: Ion Hall Parameter, calculated as the ratio of ion cyclotron frequency to ion collision frequency. The collisional cross sections used to calculate the ion collision frequency were: Ion-Neutral Charge Exchange, Ion-Neutral Elastic Scattering, and Ion-Electron Coulomb. The effects of wall recombination collisions were ignored. Including ion wall collisions would reduce the Hall parameter close to the wall. These results are from a simulation completed with the magnetic field strength reduced by a factor of 5.

An alternative representation of the degree of magnetization for each species is presented in Figures 4-4(a) and 4-4(b). Heuristically, a particle may be thought of as magnetized when its Larmor radius is much less than the dimensions of the device or features containing it. However, this picture of magnetization ignores the significant fact that the collisional frequency of a plasma must also be considered when determining the degree of magnetization of a species within a plasma. If a particle collides with other particles, or even boundaries, at a frequency much larger than its own gyrofrequency, it will not be able to execute the drifts prescribed by Equations 4.1, 4.2 and 4.3. For this reason, the Hall parameter is of

vital consideration when determining a species' degree of magnetization.

4.2 Future Work

The preliminary simulation results presented here provide a glimpse of the depth of simulated data that would become available for interpretation should a convergent simulation be successfully executed for the full magnetic field strength of the DCFT. If further attempts to run the full B case continue to fail, a new approach will be taken, such as making the permittivity factor a function in the R-Z plane, or having it vary as a function of time. Allowing γ to vary from iteration to iteration might overcome the challenges associated with the distinct transient behavior of the DCFT model, during which the number of simulated particles increases dramatically before leveling off. Even without accomplishing the simulation of a full field strength DCFT, insights into basic operating DCFT principles demonstrate the potential benefit to be gained by further computational studies. Using the data already generated in this model, a comparison between simulated ion flux to the chamber walls with existing experimental data [11] could aid in interpreting those data and offer some quantitative evidence concerning the effectiveness of DCFT erosion mitigation, and help guide future design efforts to create a lower power, longer life alternative to Hall thruster technology.

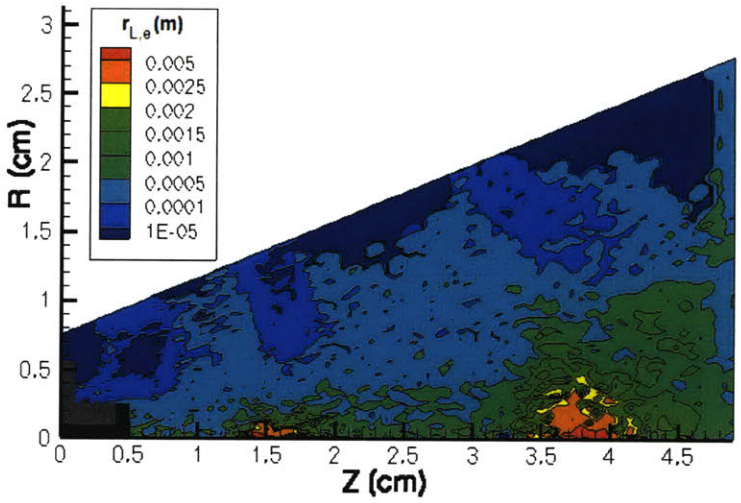

(a) Spatial variation of average electron Larmor radius. In regions where the electron density approaches zero (see Figure 3-12(a)), the Larmor radius becomes a meaningless quantity. The perpendicular velocity was taken as the bulk flow component orthogonal to the magnetic field vector.

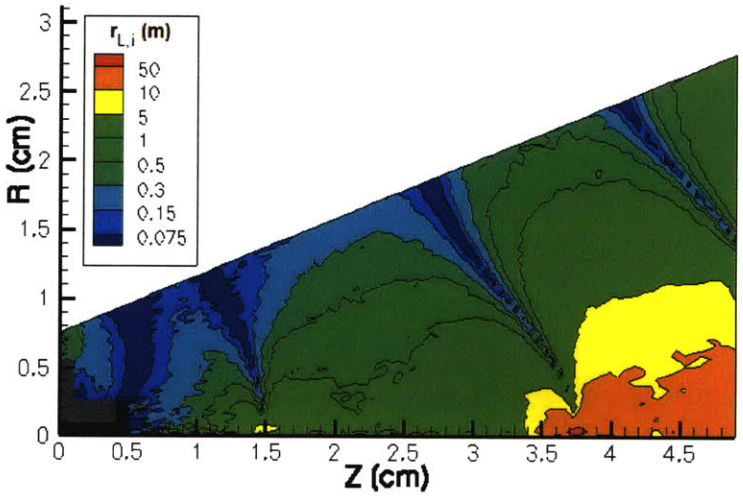

(b) Spatial variation of average ion Larmor radius. The Larmor radius is based on the component of the macroscopic ion velocity perpendicular to the magnetic field line.

Figure 4-4: Average Larmor radii for electrons and ions, calculated based on macroscopic flow velocities.

Bibliography

[1] Courtney, D. G. and Martínez-Sánchez, M., "Diverging Cusped-Field Hall Thruster (DCHT)," 30^{th} *International Electric Propulsion Conference*, FLorence, Italy, September 2007, also IEPC-2007-39.

[2] Courtney, D. G., "Development and Characterization of a Diverging Cusped Field Thruster and a Lanthanum Hexaboride Hollow Cathode," S.M. Thesis, Massachusetts Institute of Technology, Cambridge, MA, June 2008.

[3] Bober, A. S. and Kim, V., "State of Works on Electrical Thrusters in the USSR," 22^{nd} *International Electric Propulsion Conference*, Viareggio, Italy, October 1991, also IEPC-91-003.

[4] Martínez-Sánchez, M. and Pollard, J. E., "Spacecraft Electric Propulsion - An Overview," *Journal of Propulsion and Power*, Vol. 14, No. 5, 1998, pp. 688–699.

[5] Kim, V., "Main Physical Features and Processes Determining the Performance of Stationary Plasma Thrusters," *Journal of Propulsion and Power*, Vol. 14, No. 5, 1998, pp. 736–743.

[6] Courtney, D., Lozano, P., and Martínez-Sánchez, M., "Continued Investigation of Diverging Cusped Field Thruster," 44^{th} *Joint Propulsion Conference & Exhibit*, Hartford, CT, July 2008, also AIAA-2008-4631.

[7] Kornfeld, G., Koch, N., and Coustou, G., "First Test Results of the HEMP Thruster Concept," 28^{th} *International Electric Propulsion Conference*, Toulouse, France, March 2003, also IEPC–03–134.

[8] Kornfeld, G., "Plasma Accelerator Arrangement," United States Patent 6,523,338 B1, 2003.

[9] Kornfeld, G., Coustou, G., and Emsellem, G., "Plasma Accelerator System," United States Patent 7,075,095 B2, 2006.

[10] Raitses, Y. and Fisch, N. J., "Parametric Investigations of a Nonconventional Hall Thruster," *Physics of Plasmas*, Vol. 8, No. 5, 2001.

[11] Matlock, T. et al., "Spectroscopic and Electrostatic Investigation of the Diverging Cusped-Field Thruster," 45^{th} *Joint Propulsion Conference & Exhibit*, Denver, Co, August 2009, also AIAA-2009-4813.

[12] Fife, J. M., "Two-Dimensional Hybrid Particle-In-Cell Modeling of Hall Thrusters," S.M. Thesis, Massachusetts Institute of Technology, Cambridge, MA, May 1995.

[13] Fife, J. M., "Hybrid-PIC Modeling and Electrostatic Probe Survey of Hall Thrusters," Ph.D. Thesis, Massachusetts Institute of Technology, Cambridge, MA, February 1999.

[14] Szabo, J. J., "Fully Kinetic Numerical Modeling of a Plasma Thruster," Ph.D. Thesis, Massachusetts Institute of Technology, Cambridge, MA, January 2001.

[15] Blateau, V., "PIC Simulation of a Ceramic-Lined Hall-Effect Thruster," S.M. Thesis, Massachusetts Institute of Technology, Cambridge, MA, September 2002.

[16] Sullivan, K. U., "PIC Simulation of SPT Hall Thrusters: High Power Operation and Wall Effects," S.M. Thesis, Massachusetts Institute of Technology, Cambridge, MA, June 2004.

[17] Fox, J. M., "Fully-Kinetic PIC Simulations for Hall-Effect Thrusters," S.M. Thesis, Massachusetts Institute of Technology, Cambridge, MA, September 2007.

[18] Waltz, R. E., Candy, J., and Rosenbluth, M., "Gyrokinetic Turbulence Simulation of Profile Shear Stabilization and Broken GyroBohm Scaling," *Physics of Plasmas*, Vol. 9, 2002.

[19] Waltz, R. E., Dewar, R., and Garbet, X., "Theory and Simulation of Rotational Shear Stabilization of Turbulence," *Physics of Plasmas*, Vol. 5, 1998.

[20] Waltz, R. E., Staebler, G. M., Dorland, W., Hammett, G., Kotschenreuther, M., and Konings, J., "A Gyro-Landau-Fluid Transport Model," *Physics of Plasmas*, Vol. 4, 1997.

[21] Fox, J. M., "Advances in Fully-Kinetic PIC Simulations of a Near-Vacuum Hall Thruster and Other Plasma Systems," Ph.D. Thesis, Massachusetts Institute of Technology, Cambridge, MA, September 2007.

[22] Gildea, S. R., Nakles, M., Hargus, W., and Martínez-Sánchez, M., "Experimentally Characterizing the Plume of a Divergent Cusped-Field Thruster," *31st International Electric Propulsion Conference*, Ann Arbor, MI, September 2009, also IEPC-2009-259.

[23] Bittencourt, J. A., *Fundamentals of Plasma Physics*, SpringerScience & Business Media, LLC, 2004.